Astron. Astrophys. 331, 742–748 (1998)

ASTRONOMY AND ASTROPHYSICS

Detection of UIR bands in an isolated local interstellar cirrus cloud⋆

D. Lemke[1], **K. Mattila**[2], **K. Lehtinen**[2], **R.J. Laureijs**[4], **T. Liljeström**[2], **A. Léger**[3], **and U. Herbstmeier**[1]

[1] Max-Planck-Institut für Astronomie, Königstuhl 17, D-69117 Heidelberg, Germany
[2] Observatory, P.O. Box 14, FIN-00014 University of Helsinki, Finland
[3] Institut d'Astrophysique Spatiale, C.N.R.S., Université Paris XI, France
[4] ISO Science Operations Team, ESA - Villafranca, Villafranca del Castillo, Aptdo 50727, E-28080 Madrid, Spain

Received 12 June 1997 / Accepted 3 November 1997

Abstract. The unidentified infrared (UIR) emission bands at 7.7 and 11.3 μm have been detected in the emission of an isolated cirrus cloud externally heated by the typical interstellar radiation field (ISRF) of the solar neighbourhood. For the observations we used ISOPHOT, the photometer aboard ISO. The detected UIR bands have absolute intensities $\sim$ 1/1000th of the values typically observed in planetary and reflection nebulae. The intensity ratio 11.3 to 7.7 μm is at the higher end of the range observed for reflection nebulae, planetaries, HII regions, or for the diffuse emission of the inner Galaxy. An enhanced emission level is observed also in the bands 6 - 9 μm and 12 - 14 μm, suggesting the presence of the 6.2, 8.6 and 12.7 μm UIR bands. At 10 and 16 μm continuum emission has been detected which must be due to very small grains. The observations presented give further evidence that the UIR features seem to be ubiquitous throughout the galaxy. This is in support of the PAHs as carriers of the features and, moreover, as key agents in transforming the stellar UV into infrared radiation.

Key words: dust, extinction – infrared: ISM: lines and bands – Galaxy: general

1. Introduction

A surprisingly high level of mid-IR emission at 12 and 25 μm was detected by IRAS (see Boulanger et al. 1985) from many of the high latitude cirrus clouds which were most prominently seen in the IRAS 100 μm band (Low et al. 1984). This emission constitutes in many cases 20 – 30% of the total IR radiation energy of the cloud and cannot be explained as equilibrium emission by the classical dust grains. Puget et al. (1985) have proposed that the IRAS 12 μm emission of cirrus clouds is largely due to the unidentified infrared (UIR) bands. There has still been no unambiguous identification of the specific carriers of the UIR bands, the strongest of which are located at 3.3, 6.2, 7.7, 8.6, 11.3, and 12.7 μm. However, there is good evidence for the carriers being some form of carbonaceous material excited by UV photons: either large free polycyclic aromatic hydrocarbon molecules (PAHs) (Léger & Puget 1984) or grains consisting of hydrogenated amorphous carbon (HACs) (Duley & Williams 1981), quenched carbonaceous composites (QCCs) (Sakata et al. 1984), or coal (Papoular et al. 1989).

The PAH model has been supported by observations of the diffuse galactic disk emission: the photometric detection of the 3.3 μm and 6.2 μm UIR bands using the AROME balloon-borne experiment (Giard et al. 1988; Ristorcelli et al. 1994), and the ISOPHOT and IRTS spectrophotometry of the 6.2 – 11.3 μm and 3.3 – 11.3 μm UIR bands in lines of sight towards the inner Galaxy (Mattila et al. 1996, Tanaka et al. 1996, Onaka et al. 1996). Further support has been provided also by COBE/DIRBE broad band photometry of intermediate and high latitude cirrus in the 3.5 - 25 μm wavelength region (Bernard et al. 1994, 1996; Dwek et al. 1997).

The UIR emission bands have been observed in a number of bright galactic objects, such as planetary nebulae (PN), HII regions, and reflection nebulae (RN) around early type stars (Gillett et al. 1973), as well as in some external galaxies. These objects are characterized by UV radiation densities several orders of magnitude above the average interstellar radiation field (ISRF) representative of the solar neighbourhood. No spectrally resolved observations have been available so far on the near- or mid-IR emission of an individual isolated cirrus cloud.

The present investigation was initiated to answer the following questions:
(1) Are the UIR emission bands at 3.3, 6.2, 7.7, 8.6, 11.3, and 12.7 μm present also in the diffuse emission of local cirrus clouds where the UV ISRF has a typical solar neighbourhood value?

Send offprint requests to: D. Lemke (email:lemke@mpia-hd.mpg.de)

⋆ Based on observations made with ISO, an ESA project with instruments funded by ESA member states (especially the PI countries: France, Germany, the Netherlands and the United Kingdom) and with the participation of ISAS and NASA

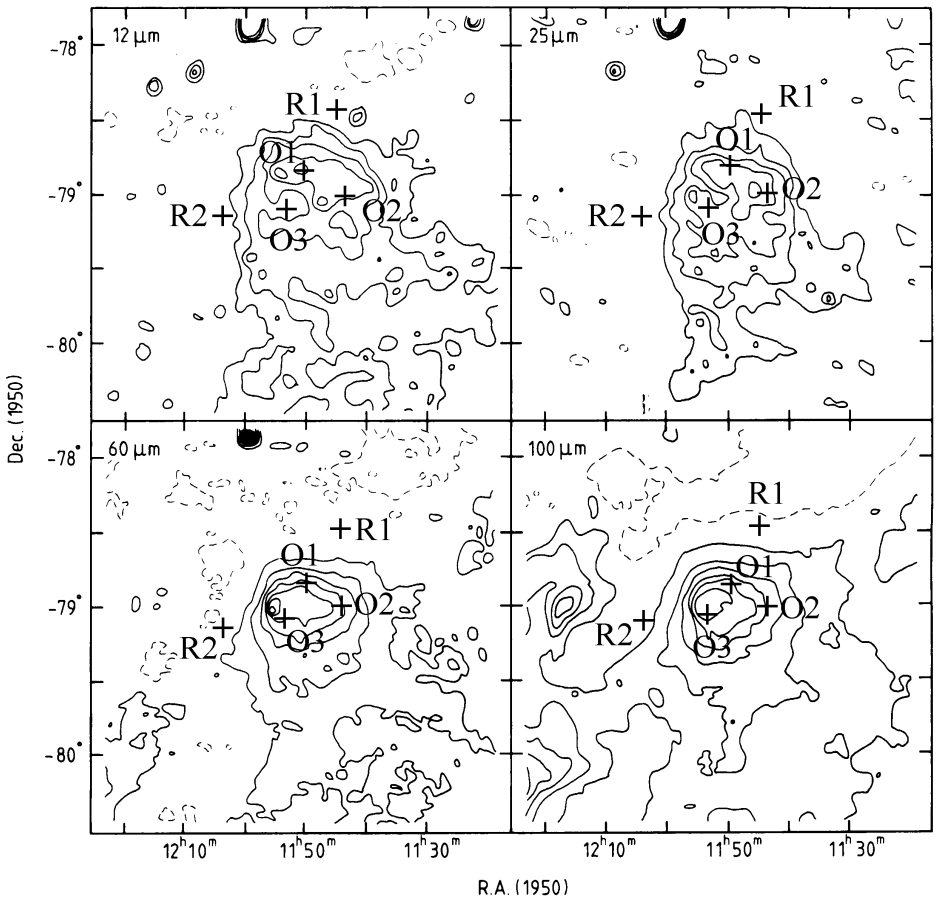

Fig. 1a–d. IRAS maps of G 300.2−16.8 (Laureijs et al. 1989) with the positions for the ISOPHOT observations. **a** 12 μm map, contour levels in steps of 0.25 MJy/sr, highest contour 1.25 MJy/sr; **b** 25 μm map, contour levels in steps of 0.25 MJy/sr, highest contour 1.25 MJy/sr; **c** 60 μm map, contour levels in steps of 0.75 MJy/sr, highest contour 5 MJy/sr; **d** 100 μm map, contour levels in steps of 3 MJy/sr, highest contour 19 MJy/sr. The ecliptic coordinates vary between $\lambda - \lambda_\odot = 102.3° - 104.6°$ ($\lambda_\odot$ for ISO revolution No. 271) and $\beta = -64.1° - 64.9°$.

(2) Can the IRAS band 1 (12 μm) cirrus emission be explained as the integrated emission of the UIR bands?
(3) What are the relative intensities of the UIR bands in comparison with the bright galactic sources, the PNs, RNs, and the HII regions?

Using ISOPHOT-P1 between 3.3 and 16 μm we observed the cirrus/translucent cloud G 300.2 − 16.8 in the Chamaeleon dark cloud complex at a distance of ∼140 – 200 pc from the sun (Franco 1991). There is recent indication that the cloud might actually be at half the distance if associated to a nearby star for which a Hipparcos determined distance had just become available. G 300.2−16.8 is characterized by a large IRAS 12/100μm ratio of 0.14 (Laureijs et al. 1989). The signal in the different IRAS bands peaks at different positions within the cloud, which indicates local dust composition changes. The relatively high galactic latitude ($b = -16.8°$) helps to avoid confusion with unrelated structures along the line of sight. Since the cirrus signal is only a few per cent of the zodiacal emission at the mid-IR wavelengths the high ecliptic latitude of G 300.2 − 16.8 ($\beta = -65°$) is an important factor in reducing noise and drift problems.

2. Observations and reductions

The observations were carried out during the ISO revolutions 271 and 276 (August 13th and 18th 1996). The observed positions are displayed in Fig. 1. The three ON positions (referred to as O1, O2, and O3) were selected to coincide with the IRAS 12, 25, and 100 μm maxima which are at clearly distinct places in the cloud. Two reference positions (R1 and R2) were selected outside the cloud.

Table 1. ISOPHOT filters used in the photometry: central wavelength λ_c, width $\Delta\lambda$, see Klaas et al. (1994). Internal and external statistical errors, σ_{int} and σ_{ext}, are given in percent of the total observed sky brightness.

Filter	λ_c (μm)	$\Delta\lambda$	$\sigma_{int}(\%)$	$\sigma_{ext}(\%)$
3.29	3.30	0.22	15	54
3.6	3.59	1.00	5	19
4.85	4.86	1.55	1	5
7.3	7.43	3.38	0.3	$\leq$3
7.7	7.64	0.84	0.8	$\leq$2
10	9.99	1.86	0.2	0.8
11.3	11.36	0.77	0.7	0.7
12.8	12.83	2.33	0.2	0.6
16	15.14	2.86	0.4	0.3

The observations were performed in nine filters which are listed in Table 1. Aperture size was 180″, the integration time was 64 sec for the 3.29, 3.6, and 4.85 μm filters and 32 sec for the others. The sparse map Observing Templates (AOTs

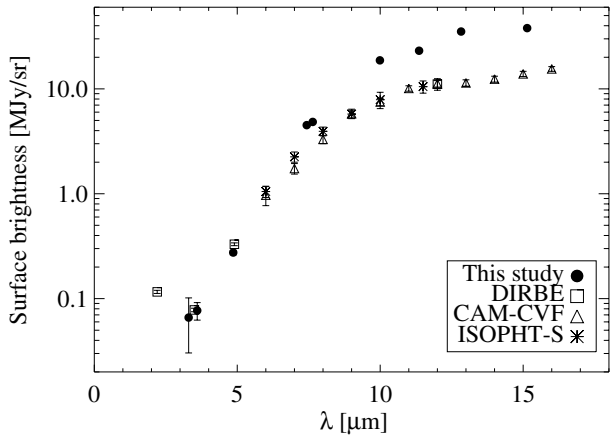

Fig. 2. Zodiacal emission in the direction of G 300.2 − 16.8 reference position R2, (see Fig. 1) measured with 3.29 – 16 μm filters and using the (default) P1 detector responsivity of 1.05 A/W. For comparison the zodiacal emission spectra as measured by DIRBE, ISOCAM-CVF, and ISOPHOT-S, and reduced to the position of G 300.2 − 16.8 are shown. These values are adopted to calibrate the measurements of this study. The error bars for the G 300.2 − 16.8 measurements indicate (external) statistical errors only.

PHT17/18/19) were used (Klaas et al. 1994). A separate sparse map was performed in each filter. In this observing mode the detector remains switched on during the whole measuring cycle. Since the sky brightness changes only a few per cent between the different ON- and REF-positions in a map this method minimizes drift effects.

The first and the last observation of each sparse map were followed by a measurement of the on board calibration source FCS1 (Lemke et al. 1996), which was heated to give a signal corresponding to the expected sky brightness. Presently, the FCS calibration for the large apertures has not been completed. Therefore, in this analysis we have used the zodiacal emission as calibration source. We show in Fig. 2 the zodiacal emission spectrum between 2.2 and 16 μm. Three different measurements were used: (1) ISOPHOT-S observation at $\lambda - \lambda_\odot = 67°$, $\beta = -5°$ calibrated with standard stars (HR 6705 and HR 6688) to an absolute accuracy of $\sim$20% (Ábrahám et al. 1997); (2) ISOCAM-CVF observation at $\lambda - \lambda_\odot = 104.3°$, $\beta = -2.4°$ (Reach et al. 1996); and (3) COBE/DIRBE observation at the south ecliptic pole (Hauser 1996). All spectra were scaled to the position $\lambda - \lambda_\odot = 103.8°$, $\beta = -64.7°$, applying the well established global brightness distribution of the zodiacal light (see Leinert et al. 1997).

We also show in Fig. 2 the results of our ISOPHOT-P1 photometry at the position R2 near G 300.2 − 16.8. We have used from each sparse map the last reference position measurement for which the detector drift effects are minimized (see Fig. 3). The default detector responsivity (1.05 A/W) has been adopted for the G 300.2 − 16.8 data points displayed in Fig. 2. It can be seen that while the *shape* of our measured ISOPHOT-P1 zodiacal emission spectrum is similar to the DIRBE/ISOCAM-CVF/ISOPHOT-S spectrum there are differences from filter to filter and the *absolute* level is higher at the longer wavelengths. Based on the comparison with the zodiacal emission spectrum we have thus adopted a responsivity correction for each filter, i.e. we use the reliable zodiacal emission values to calibrate our measurements. This method is further justified by the calibration of the signal dependence on aperture size available so far only for the 11.5 μm filter. Applying the correction factor of 0.55 between stellar calibrations in the 53″ aperture and the 180″ aperture used here, together with the actual responsivity of 2.16 A/W of the FCS calibration, gives good agreement between both methods.

The data reduction was performed using the ISOPHOT Interactive Analysis programme (PIA) Version V5.1 (Gabriel et al. 1996). The following reduction steps were applied:
(1) Correction for non-linearity of the signal integration ramps
(2) Deglitching of the data (to eliminate cosmic ray effects)
(3) Deletion of first $\sim$10 sec of integration (to eliminate detector drift effects)
(4) Subtraction of dark current
(5) Calibration to convert instrumental units (V/s) to surface brightness (MJy/sr)
(6) Correction for the detector drift
(7) Subtraction of the zodiacal emission by using the measurements at the reference positions.

We display the calibrated measurements for the nine sparse maps in Fig. 3. For the six filter bands between 7.3 and 16.0 μm there is a clear excess signal in the ON positions whereas for the three bands at 3.29, 3.6, and 4.85 μm only an upper limit can be derived. The detector drift has been modelled by fitting through the reference position data points a curve of the form $F_\nu = a/(e^{-bt} + c)$ where F_ν is the surface brightness and t is the time elapsed since the beginning of the sparse map.

After correction with this fitted line the final spectra of cirrus emission at the three ON positions are obtained and are shown in Fig. 4. Based on this observed energy distribution, modelling of the UIR band emission becomes possible, if gaussian profiles are assumed for the spectral features observed in other galactic emission regions. At the 3.29 μm feature, however, only an upper limit was detected and no separate 6.2 μm band measurement is available. Therefore a model spectrum would not be unique and its presentation is suppressed here.

Statistical errors have been estimated by two methods: (1) internal errors for each measurement are obtained from the PIA analysis; (2) external errors are obtained from comparison of two independent measurements for O1, O2, O3 at λ = 10, 11.3, 12.8, and 16 μm, and from comparison of all ON and REF point measurements at 3.29, 3.6, and 4.84 μm. At 7.3 and 7.7 μm only one measurement was available for each ON position; upper limits for external errors were estimated from the scatter of these values. Estimates of the internal and external statistical errors are given in Table 1. *Relative filter-to-filter calibration* errors depend on the accuracy of the zodiacal emission spectral *shape* and the statistical accuracy of the G 300.2 − 16.8 R2 measurements used in the calibration (see Fig. 2). We estimate that this accuracy is $\pm$10%. The *absolute calibration accuracy* depends also on the absolute zodiacal emission brightness. Ad-

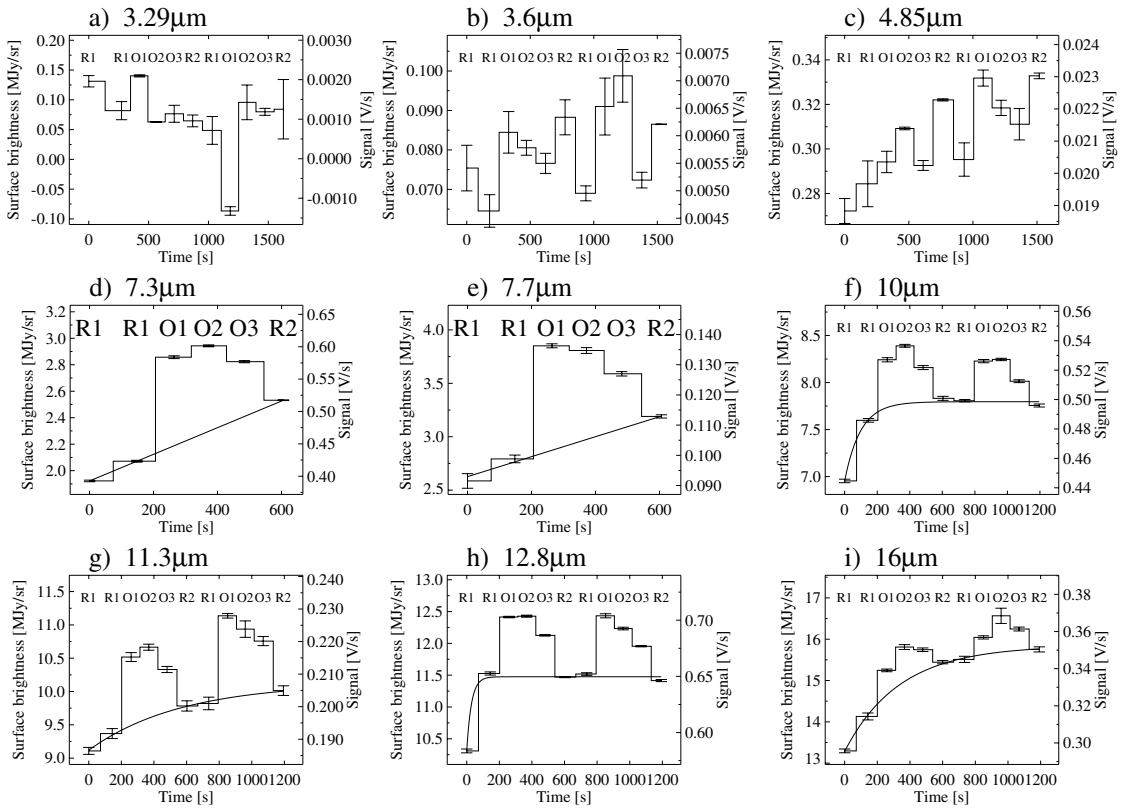

Fig. 3. Observed surface brightness in the nine different ISOPHOT filters. The on target and reference positions are designated as O1, O2, O3 and R1, R2, respectively. The measured values are plotted in the same sequence as they were measured in each sparse map. For the 7.3 – 16 μm measurements a fitted curve representing the detector drift is shown as well. The values at R1 and R2 represent the zodiacal light brightness. The surface brightness is given both in the instrumental (V/s) and physical units (MJy/sr). The error bars are internal statistical errors as obtained from the standard PIA reductions. The time constants of the detector drift curves depend on the signal level (V/s), being smaller when the signal is larger.

Table 2. The integrated emission 7.5 – 15.0 μm as observed with ISOPHOT and the IRAS in-band fluxes at 12, 25, 60, and 100 μm. All values are relative to a zero point determined at the reference positions. Error estimates are given in the last line. The last column gives the ratio of the 12 and 100 μm IRAS in-band fluxes.

Position	ISOPHOT	IRAS				
	7.5-15 μm	12	25	60	100	$\frac{12}{100}$
	(10^{-11} W cm^{-2} sr^{-1})					
O1	1.7	1.5	0.46	0.62	0.99	1.5
O2	1.6	1.4	0.72	0.90	1.3	1.1
O3	1.0	0.8	0.46	1.2	2.0	0.4
	±30%	±15%		±30%		

ditional information is provided by comparison with IRAS 12 μm emission measured at the positions O1, O2, O3 (see Sect. 3). We estimate that the absolute calibration is accurate to ±30%.

3. Results

In order to compare the emission detected by ISOPHOT with the emission in the IRAS 12 μm band (7.5 to 15.0 μm) we have summed up our values at 7.3, 10, 11.3, 12.8, and 16 μm (multiplied with appropriate weights). The in-band fluxes thus determined for the 7.5 - 15 μm wavelength band are given in Table 2 together with the IRAS in-band values for the 12, 25, 60, and 100 μm bands. As the comparison shows, similar values are obtained for the 7.5 - 15 μm emission both by ISOPHOT and IRAS. This provides a further confirmation for our flux calibration.

The observed in-band power of the cirrus emission at the three ON positions is given in Table 3. For the three shortest wavelengths only upper limits could be derived. They correspond to 2σ deviations from a fitted first or second order polynomial through all (ON and REF) data points of the sparse maps as shown in Fig. 3. In order to estimate the contributions of the UIR bands we have assumed a flat continuum, F_λ = const, between 6 – 10 μm, i.e we have used the observed continuum at 10 μm for the 7.3 and 7.7 μm filter bands. For the 11.3 and 12.8 μm filter bands we have interpolated the continuum linearly between the 10 and 16 μm observations. For the 3.29 μm filter the same upper limit as in Table 3 is given. The resulting in-band emission of the UIR features in the bands 3.29, 7.3, 7.7, 11.3, and 12.8 μm are given in columns (2) – (6) of Table 4. In column (7) we give the total emission power (bands + continuum) be-

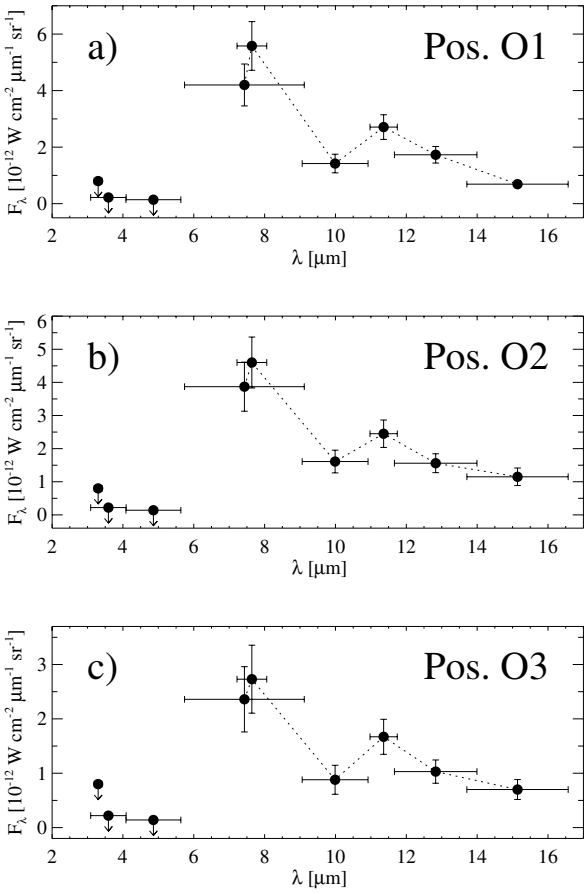

Fig. 4a–c. The observed spectral energy distributions of the cirrus emission at the three IRAS peaks in G 300.2 − 16.8: **a** 12 μm (= O1); **b** 25 μm (= O2); **c** 100 μm (= O3). The filter widths and flux errors are indicated by horizontal and vertical bars. The errors include (external) statistical errors and filter-to-filter relative calibration errors (10%). For the three shortest wavelengths 2σ upper limits are shown.

tween 6 – 16.5 μm. The contribution by UIR bands is 38 to 52% of the total emission in the 6 – 16.5 μm band (see Table 4). In column (8) we list the ratio of the UIR band contribution to the total emission power and in columns (9), (10), and (11) we give the UIR band ratios P(11.3)/P(7.7), [P(11.3) + P(12.8)]/P(7.3), and P(3.29)/P(11.3), respectively.

Based on the spectral energy distributions for the three positions in G 300.2 − 16.8 (see Fig. 4 and Tables 3 and 4) we infer the following results:
(1) The excess emission in the 7.7 and 11.3 μm narrow filter bands indicates the presence of these UIR bands. The band ratio P(11.3)/P(7.7) = 0.33 – 0.43 is within the range found for the high-ISRF objects.
(2) The broad-band 7.3 μm filter indicates an integrated UIR band emission between 6 - 9 μm by factor $\sim$3 larger than the power in the 7.7 μm band. Thus, in addition to the 7.7 μm band, contributions by the UIR bands at 6.2 and 8.6 μm and/or the broad plateau emission between 6 and 9 μm are suggested.
(3) A contribution of the 12.7 μm band is suggested by the enhanced level of the 12.8 μm filter.
(4) An upper limit to the 3.3 μm UIR band is obtained. For position O1 the band ratio P(3.3)/P(11.3) is $\leq$ 0.14 which is marginally compatible with those of high-ISRF objects.
(5) Continuum emission is detected at 10 and 16 μm in all three spectra. At 3.6 and 4.85 μm only an upper limit to the continuum can be determined. Over the wavelength region 6 – 16 μm the contribution of the continuum emission is roughly equal to the emission power in the bands. There are distinct differences in the slopes of the 10 – 16 μm continuum between the three positions.
(6) The absolute level of the average UIR band emission in the 7.7 μm filter is $\sim$3 10^{-12} W cm^{-2} μm^{-1} sr^{-1} which is by a factor $\sim$ 10^3 fainter than in typical RNs or HII regions (e.g. NGC 2023, Orion Bar).
(7) The ratio of the integrated emission powers (in W cm^{-2} sr^{-1}) of the two UIR band groups at 11 - 14 and 6 – 9 μm is measured between 0.23 and 0.31 and is within the range found for the high ISRF objects.

4. Discussion

4.1. PAH energy budget

Some 20 to 30% of the total IR-emission of a typical cirrus cloud is emitted by transiently heated very small particles in the 12 and 25 μm IRAS bands (see e.g. Boulanger et al. 1985, Laureijs et al. 1989, Bernard et al. 1994, Dwek et al. 1997). We have estimated the total infrared emission 6 – 1000 μm for the three positions in G 300.2 − 16.8 . Besides the ISOPHOT photometry we have utilised the 25, 60, and 100 μm IRAS data and, for extrapolation beyond 100 μm, the spectral energy distribution as derived by Dwek et al. (1997) from the COBE/DIRBE and FIRAS data. The resulting values are 1.5 (O1), 1.3 (O2), and 2.5 10^{-10} W cm^{-2} sr^{-1} (O3). Using the data in column (7) and (8) of Table 4 we find that the UIR bands contain a fraction of 5 – 6% and 2% of the total IR-emission at positions O1, O2 and O3, respectively. Very small particles emit a fraction of 20 – 40% of the total at O1, O2 and $\sim$10% at O3, the exact percentage depending on the maximum wavelength (16.5 or 30 μm) adopted for the very small particle emission. We conlude that the carriers of the UIR bands are an important agent in cirrus clouds processing stellar UV radiation energy into IR-emission.

4.2. Band ratios and PAH properties

A basic result of our observations is that the relative intensities of the UIR bands in G 300.2 − 16.8 are comparable to those in the high-ISRF objects (see Table 4). There is a longstanding problem with the explanation of the UIR band intensities in terms of the PAH hypothesis. For neutral, hydrogenated PAHs the bands around 11 – 13 μm which are due to C – H out-of-plane bending vibrations are stronger than the 6.2 and 7.7 μm C – C stretching bands. In highly UV irradiated objects like RNs, HII regions and PNs the contrary situation is observed. This now also seems

Table 3. The in-band emission power of the cirrus cloud (bands + continuum) as observed with ISOPHOT in the different filter bands. The values are relative to a zero level determined at the reference positions. The error estimates given in parentheses include (external) statistical errors and a 10% calibration error. The unit is 10^{-12} W cm^{-2} sr^{-1}.

Position	P(3.29)	P(3.6)	P(4.85)	P(7.3)	P(7.7)	P(10)	P(11.3)	P(12.8)	P(16)
O1	$\leq$0.18	$\leq$0.27	$\leq$0.31	14.2(2.8)	4.34(0.7)	2.54(0.6)	2.08(0.3)	3.78(0.7)	1.85(0.3)
O2	$\leq$0.18	$\leq$0.27	$\leq$0.31	13.0(2.8)	3.58(0.7)	2.88(0.6)	1.88(0.3)	3.40(0.6)	3.08(0.4)
O3	$\leq$0.18	$\leq$0.27	$\leq$0.31	8.0(2.1)	2.12(0.5)	1.58(0.5)	1.28(0.2)	2.25(0.4)	1.86(0.3)

Table 4. The in-band emission power of UIR bands as observed with ISOPHOT in the different filter bands (columns 2 – 6). The values are relative to a continuum level as explained in the text. The error estimates given in parentheses include (external) statistical errors and a 10% calibration error. The unit is 10^{-12} W cm^{-2} sr^{-1}. Column (7) gives the total emission power (bands + continuum) in the 6 – 16.5 μm region. Columns (8) – (11) give bands-to-total and three different band ratios. In the lower part of the table values from literature are given for comparison: diffuse emission of the galactic disk (DGBE), Mattila et al. (1996), Onaka et al. (1996), Tanaka et al. (1996); ρ Oph, Boulanger et al. (1996); RN, PN, HII regions, see Cohen et al. (1989), Roelfsma et al. (1996), Cesarsky et al. (1996), Verstraete et al. (1996).

Position	P(3.29)	P(7.3)	P(7.7)	P(11.3)	P(12.8)	Total	$\frac{Bands}{Total}$	$\frac{P(11.3)}{P(7.7)}$	$\frac{P(11.3)+P(12.8)}{P(7.3)}$	$\frac{P(3.29)}{P(11.3)}$
	(2)	(3)	(4)	(5)	(6)	(7)	(8)	(9)	(10)	(11)
O1	$\leq$0.18	8.96 (3.1)	3.19 (0.8)	1.28 (0.4)	1.55 (0.9)	22.8 (3.0)	0.52 (0.16)	0.40 (0.15)	0.31 (0.15)	$\leq$0.14
O2	$\leq$0.18	7.19 (3.0)	2.27 (0.8)	0.76 (0.4)	0.87 (0.8)	23.0 (3.0)	0.38 (0.14)	0.33 (0.19)	0.23 (0.17)	$\leq$0.24
O3	$\leq$0.18	4.91 (2.3)	1.45 (0.5)	0.63 (0.3)	0.55 (0.7)	14.1 (2.2)	0.43 (0.18)	0.43 (0.25)	0.24 (0.19)	$\leq$0.29
DGBE		410	200	53		470[a]	$\sim$1	0.26		$\sim$0.06
ρ Oph		157	97	27	32	700	0.31	0.28	0.38	
RN,PN,HII						12600[b]		0.09-0.47	0.24-0.74	0.15-0.43

a) for 5.8 - 11.6 μm

b) for 6 - 15 μm, NGC 7023 (Laureijs et al. 1996)

to be indicated in the diffuse cloud G 300.2 − 16.8 located in the weak ISRF. A possible explanation for the small 11.3/7.7 μm ratio in these environments is that the PAHs are strongly dehydrogenated (see Léger et al. 1989). Since dehydrogenation is expected to be much weaker for a cirrus cloud, a substantially larger 11.3/7.7 μm ratio would be expected for G 300.2 − 16.8 which is *not* the case. We conclude that our observations do not support dehydrogenation as a solution to the band ratio problem.

A probable solution to this problem has emerged from recent laboratory and theoretical results for cross sections of singly ionized PAHs (PAH$^+$) (for a review see Allamandola et al. 1995). The 6.2, 7.7 and 8.6 μm band cross sections for PAH$^+$s are typically a factor of 10 larger than for neutral PAHs. The observed 11.3/7.7 μm ratio (Table 4) could thus be understood if a substantial fraction of the PAHs are ionized not only in the high-ISRF objects but also in G 300.2 − 16.8. The ionisation degree results from an equilibrium between ionizing events, depending on the intensity of the ISRF, and recombination events, depending on the local electron density (Omont 1986). In regions with high UV radiation density and low electron density, such as RNs, the fraction of ionized PAHs approaches unity. In the local-ISRF diffuse medium the situation is less clear. Verstraete et al. (1990) have estimated that for the two compact PAHs, coronene and pyrene, the ionization degree ([PAH$^+$]/[PAH]) is $\sim$6%. For the same PAH molecules Bakes & Tielens (1994) and Salama et al. (1996) have calculated similarly low [PAH$^+$]/[PAH] ratios in moderately dense ($n_{\rm H} \gtrsim 200$ cm^{-3}) diffuse clouds. Joblin et al. (1996) have found that the 8.6/11.3 μm ratio in the reflection nebula NGC 1333 decreases by a factor of $\sim$2 between the position of the star and outer nebula in accordance with the calculated change of ionization degree. A similar result has been obtained in NGC 7023 by Cesarsky et al. (1996) for the band ratios of the 6.2 – 8.6 μm and 11.3 – 12.7 μm groups. As a consequence, we would expect the 11.3/7.7 μm ratio to be higher in the low-ionization environment of G 300.2 − 16.8 than in the reflection nebulae with $\sim$100% PAH ionization. Although the value for G 300.2 − 16.8 is at the upper end of the wide range obtained for RN, PN and HII, it is not clear whether this can already be considered as a significant effect, given the variation and uncertainties of values now obtained for the cirrus cloud.

The continuum emission in the 10 and 16 μm bands may be explained by two alternative models: (1) non-equilibrium emission by large clusters of PAH molecules or very small carbonaceous grains (see e.g. Schutte et al. 1993, Moutou et al. 1996); (2) non-equilibrium emission by very small silicate grains (Draine & Anderson 1985, see also discussion in Désert et al. 1986). Any *equilibrium emission* by large grains at $\lambda \leq 16\mu$m is *excluded* due to the weak ISRF and thus low temperature ($T < 50$ K) of such grains in the cirrus. We notice that the 10 μm continuum flux is higher by a factor of $\sim$2 at O1 and O2 than at O3. The 16 μm continuum has its maximum value at O2 (IRAS 25 μm peak) while the emission levels at O1 (IRAS 12 μm peak) and O3 (IRAS 100 μm peak) are equal. This suggests that the 16 μm emission, if due to PAHs, is at least partially caused by a different population of the size distribution (larger species).

5. Conclusions

The observations had for the first time sufficient sensitivity to analyse the mid infrared emission of a single interstellar cirrus

cloud exposed to the local ISRF. The main results of the observations can be summarized as follows:
(1) We have detected the UIR bands at 7.7 and 11.3 μm.
(2) Additional emission bands seem to be present between 6 – 9 μm and 11.5 – 14 μm.
(3) A continuum emission is observed in the 10 and 16 μm filterbands. It accounts for about half of the emission between 6 and 16.5 μm.
From an analysis of the band intensities and ratios we have derived the following conclusions:
(1) The UIR band carriers in cirrus clouds are effective transformers for stellar UV radiation into IR emission throughout the galaxy. The similarity of the measured emission spectra in the faint cirrus cloud G 300.2 − 16.8 and in planetary and reflection nebulae with a thousandfold higher irradiation level excludes any equilibrium emission by large dust grains. It rather suggests the presence of the so called interstellar PAHs also in cirrus clouds.
(2) The 11.3/7.7 μm band ratio is $\sim$0.3 – 0.4, i.e. substantially lower than predicted for neutral hydrogenated PAHs exposed to the ISRF of the solar neighbourhood. We have presented arguments that the ratio observed can be understood in terms of the PAHs being partially ionized.

Acknowledgements. We gratefully acknowledge the funding of the ISOPHOT experiment by the Deutsche Agentur für Raumfahrtangelegenheiten (DARA) and financial support for this research project by the Max-Planck Society, the University of Helsinki Research Fund, and the Academy of Finland (Grant No. 1011055). We are grateful to members of the ISOPHOT Data Centre at MPIA, Heidelberg, for help during the data analysis as well as to members of the ISOPHOT Instrument Dedicated Team at VILSPA for support in the calibration of the wide beams.

References

Ábrahám, P., Leinert, C., Lemke, D. et al., 1997, A&A (in preparation)
Allamandola, L.J., Sandford, S.A., Hudgins, D.M., Witteborn, F.C., 1995, PASP Conf. Ser. 73, 23
Bakes, E.L.O., Tielens, A.G.G.M., 1994, ApJ 427, 822
Bernard, J.-P., Boulanger, F., Désert, F.X. et al., 1994, A&A 291, L5
Bernard, J.-P., Boulanger, F., Désert, F.X. et al., 1996, Dust in the diffuse ISM as revealed by DIRBE observations, In: Dwek, E. (ed.) Unveiling the Cosmic Infrared Background, AIP Conf. Proc. 348, p. 105
Boulanger, F., Baud, B., van Albada, G.D., 1985, A&A 144, L9
Boulanger, F., Reach,W.T., Abergel, A. et al., 1996, A&A 315, L325
Cesarsky, D., Lequeux, J., Abergel, A. et al. 1996, A&A 315, L305
Cohen, M., Tielens, A.G.G.M., Bregman, J.D. et al., 1989, ApJ 341, 246
Désert, F.X., Boulanger, F., Léger, A. et al., 1986, A&A 159, 328
Duley, W.W., Williams, D.A., 1981, MNRAS 196, 269
Draine, B.T., Anderson, N., 1985, ApJ 292, 494
Dwek, E., Arendt, R.G., Fixsen, D.J. et al., 1997, ApJ 475, 565
Franco, G., 1991, A&A 251, 581
Gabriel, C., Haas, M., Heinrichsen, I., Tai, W.-M., 1996, The ISOPHOT Interactive Analysis – PIA User Manual
Giard, M., Pajot, F., Lamarre, J.M. et al., 1988, A&A 201, L1
Gillett, F.C., Forrest, W.J., Merrill, K.M., 1973, ApJ 183, 87
Hauser, M.G., 1996, Searching for the Cosmic Infrared Background. In: Dwek, E. (ed.) Unveiling the Cosmic Infrared Background, AIP Conf. Proc. 348, p. 11
Joblin, C., Tielens, A.G.G.M., Geballe, T.R., Wooden, D., 1996, ApJ 460, L119
Klaas, U., Krüger, H., Heinrichsen, I., Heske, A., Laureijs, R. (eds) 1994, ISOPHOT Observers Manual, version 3.1
Laureijs, R.J., Chlewicki, G., Clark, F.O., Wesselius, P.R., 1989, A&A 220, 226
Laureijs, R.J., Acosta-Pulido, J., Ábrahám, P. et al., 1996, A&A 315, L313
Léger, A., Puget, J.L., 1984, A&A 137, L5
Léger, d'Hendecourt, L., Défourneau, D., 1989, A&A 216, 148
Leinert, C., Bowyer, S., Haikala, L. et al., 1997, A&AS (in print)
Lemke, D., Klaas, U., Abolins, J. et al., 1996, A&A 315, L64
Low, F.J., Beintema, D.A., Gautier, T.N. et al., 1984, ApJ 278, L19
Mattila, K., Lemke, D., Haikala, L. et al., 1996, A&A 315, L353
Moutou, C., Léger, A., d'Hendecourt, L., 1996, A&A 310, 297
Omont, A., 1986, A&A 164, 159
Onaka, T., Yamamura, I., Tanabé, T., Roellig, T.L., Yuen, L, 1996, PASJ 48, L59
Papoular, R., Conrad, J., Giuliano, M., Kister, J., Mille, G., 1989, A&A 217, 204
Puget, J.L., Léger, A., Boulanger, F., 1985, A&A 142, L19
Reach, W.T., Abergel, A., Boulanger, F. et al., 1996, A&A 315, L381
Ristorcelli, I., Giard, M., Meny, C. et al., 1994, A&A 286, L23
Roelfsema, P.R.; Cox, P., Tielens, A.G.G.M. et al., 1996, A&A 315, L298
Sakata, A., Wada, S., Tanabe, T., Onaka, T., 1984, ApJ 287, L51
Salama, F., Bakes, E.L.O., Allamandola, L.J., Tielens, A.G.G.M., 1996, ApJ 458, 621
Schutte, W.A., Tielens, A.G.G.M., Allamandola, L.J., 1993, ApJ 415, 397
Tanaka, M., Kawada, M., Matsumoto, T. et al, 1996, PASJ 48, L53
Verstraete, L., Léger, A., d'Hendecourt, L., Dutuit, O., Défourneau, D., 1990, A&A 237, 436
Verstraete, L., Puget, J.L., Falgarone, E. et al. 1996, A&A 315, L337

This article was processed by the author using Springer-Verlag LaTeX A&A style file *L-AA* version 3.